Sparse and optimal acquisition design for diffusion MRI and beyond

Cheng Guan Koay[a)]
Department of Medical Physics, University of Wisconsin School of Medicine and Public Health, Madison, Wisconsin 53705

Evren Özarslan
Section on Tissue Biophysics and Biomimetics, PPITS, NICHD, National Institutes of Health, Bethesda, Maryland 20892 and Center for Neuroscience and Regenerative Medicine, Uniformed Services University of the Health, Sciences, Bethesda, Maryland 20814

Kevin M. Johnson
Department of Medical Physics, University of Wisconsin School of Medicine and Public Health, Madison, Wisconsin 53705

M. Elizabeth Meyerand
Department of Medical Physics, University of Wisconsin School of Medicine and Public Health, Madison, Wisconsin 53705 and Department of Biomedical Engineering, University of Wisconsin-Madison, Madison, Wisconsin 53705

(Received 3 January 2012; accepted for publication 29 February 2012; published 16 April 2012)

Purpose: Diffusion magnetic resonance imaging (MRI) in combination with functional MRI promises a whole new vista for scientists to investigate noninvasively the structural and functional connectivity of the human brain—the human connectome, which had heretofore been out of reach. As with other imaging modalities, diffusion MRI data are inherently noisy and its acquisition time-consuming. Further, a faithful representation of the human connectome that can serve as a predictive model requires a robust and accurate data-analytic pipeline. The focus of this paper is on one of the key segments of this pipeline—in particular, the development of a sparse and optimal acquisition (SOA) design for diffusion MRI multiple-shell acquisition and beyond.
Methods: The authors propose a novel optimality criterion for sparse multiple-shell acquisition and quasimultiple-shell designs in diffusion MRI and a novel and effective semistochastic and moderately greedy combinatorial search strategy with simulated annealing to locate the optimum design or configuration. The goal of the optimality criteria is threefold: first, to maximize uniformity of the diffusion measurements in each shell, which is equivalent to maximal incoherence in angular measurements; second, to maximize coverage of the diffusion measurements around each radial line to achieve maximal incoherence in radial measurements for multiple-shell acquisition; and finally, to ensure maximum uniformity of diffusion measurement directions in the limiting case when all the shells are coincidental as in the case of a single-shell acquisition. The approach taken in evaluating the stability of various acquisition designs is based on the condition number and the A-optimal measure of the design matrix.
Results: Even though the number of distinct configurations for a given set of diffusion gradient directions is very large in general—e.g., in the order of 10^{232} for a set of 144 diffusion gradient directions, the proposed search strategy was found to be effective in finding the optimum configuration. It was found that the square design is the most robust (i.e., with stable condition numbers and A-optimal measures under varying experimental conditions) among many other possible designs of the same sample size. Under the same performance evaluation, the square design was found to be more robust than the widely used sampling schemes similar to that of 3D radial MRI and of diffusion spectrum imaging (DSI).
Conclusions: A novel optimality criterion for sparse multiple-shell acquisition and quasimultiple-shell designs in diffusion MRI and an effective search strategy for finding the best configuration have been developed. The results are very promising, interesting, and practical for diffusion MRI acquisitions.
[http://dx.doi.org/10.1118/1.3700166]

Key words: sparse design, optimal acquisition, diffusion MRI, multiple-shell acquisition, 3D radial MRI, moderately greedy combinatorial search, combinatorial optimization

I. INTRODUCTION

Diffusion magnetic resonance imaging (MRI),[1–3] a noninvasive and nonionizing magnetic resonance imaging technique, is one of the most exciting and promising imaging techniques and is increasingly being used in basic neuroscience research and clinical studies of neurological diseases.[4–8] Diffusion MRI in combination with functional MRI (Ref. 9) promises a whole new vista for scientists to explore the human brain from structural and functional connectivity to

human cognition. Such an exploration in human inquiry had heretofore been out of reach.

Diffusion MRI data are inherently noisy and its acquisition time-consuming. Hence, a faithful representation of the human connectome[10,11] that can serve as a predictive model for scientists to make inferences and discoveries requires a robust and accurate data-analytic pipeline[12–17] from data acquisition, data processing to data visualization, and data reduction. Here, our focus will be on the sparse and optimal acquisition (SOA) design for diffusion MRI, especially in the context of multiple-shell acquisition.

Diffusion tensor imaging (DTI) (Ref. 3) is the most commonly used variant of diffusion MRI techniques[18–25] in clinical studies, and consequently, the acquisition design of DTI has also been investigated extensively.[26–31] However, these investigations[26–31] focused mainly on a very special acquisition, which is known as a single-shell acquisition in which the diffusion gradient directions can be conceptualized as vectors that are antipodally symmetric and are also distributed uniformly on some spherical shell because a single diffusion weighting (also known as b-value) is employed in the acquisition (without counting the nondiffusion weighted measurements). With the emerging interests in compressive sensing (CS) methodology in imaging sciences,[32–34] the question and problem of constructing a SOA design will surely be of significant interest because CS unified the notions of sparsity in signal representation and of incoherence in sampling in a novel attempt to unravel the problem of finding the sparsest signal under the condition of underdetermined set of measurements. We should note that our goal here is to construct a SOA design that is sparse and maximally incoherent in sampling so as to achieve low coherent with respect to the typical bases used in 3D reconstruction of diffusion propagator, see e.g., Refs. 35–37. Maximum incoherence in sampling is a desirable sampling strategy and is related to uniformity of the diffusion gradient vectors (or measurements) in angular sampling for a single-shell acquisition.

Even though we briefly touched on the issue of and a simple solution to optimal ordering for multiple-shell acquisitions in our recent work,[31] we left the question regarding the optimal placements of diffusion gradient directions across and within spherical shells unaddressed because of the inherent complexity of the problem of maximizing the incoherence for a given number of measurements on these spherical shells, which is a combinatorial optimization of substantial complexity due to enormous number of distinct configurations, e.g., 10^{27} to more than 10^{232} for diffusion MRI and $10^{46\ 642}$ for three-dimensional radial MRI, see Appendix A. The focus of this work is to provide a novel and practical solution to the problem of SOA design in diffusion MRI.

Multiple-shell acquisition, which is not uncommon in DTI studies, is increasingly being used in other diffusion MRI techniques[36,38] but the search for its optimality criterion has been elusive. In this work, we propose a novel optimality criterion for sparse multiple-shell and quasimultiple-shell acquisition designs in diffusion MRI and an effective semistochastic and moderately greedy combinatorial search strategy with simulated annealing[39] to locate the optimum design or configuration.

Our proposed method determines the optimal sampling pattern for multiple-shell acquisition or quasimultiple-shell acquisitions through optimization of a cost function once the required parameters, specifically the number of shells (or b-values[3] or q-values[8,40]) and the number of measurements in each shell, are provided. The cost function directly incorporates the criteria to (1) maximize uniformity of the diffusion measurements in each shell, which is equivalent to maximal incoherence in angular measurements, (2) maximize coverage of the diffusion measurements around each radial line to achieve maximal incoherence in radial measurements for quasimultiple-shell acquisition, and finally (3) ensure maximum uniformity of diffusion measurement directions in the limiting case when all the shells are coincidental as in the case of a single-shell acquisition. The results are very exciting and promising, and they showed that the search strategy is very effective in finding the optimum configuration. Further, it was found that the square design is the most robust (i.e., with stable condition numbers and A-optimal measure across varying experimental conditions) among many other possible designs of the same sample size. Note that the lower the A-optimal measure the lower the mean squared error of the model.[41]

II. THEORY

Suppose that we have the required parameters such as the number of shells, denoted by K, and the number of measurements in each shell, i.e., jth shell has n_j number of measurements so that the total number of measurements, denoted by N, is given by $N = \sum_{i=1}^{K} n_i$.

To construct a cost function that directly incorporates the following criteria:

1. maximize uniformity of the diffusion measurements in each shell;
2. maximize coverage of the diffusion measurements around each radial line;
3. ensure maximum uniformity of diffusion measurement directions in the limiting case when all the shells are coincidental as in the case of a single-shell acquisition,

we will first deal with criterion #3 by having all N measurements uniformly distributed on the upper hemisphere of unit radius (or antipodally symmetric points on the whole sphere). This strategy ensures sufficient angular coverage in the case of multiple-shell or quasi-multiple-shell acquisitions and maximum angular coverage in the limit when the shells are coincidental as in the case of a single-shell acquisition. Note that, criteria #2 and #3 would be incompatible if we were to maximize coverage of the diffusion measurements *along* rather than *around* each radial line. We should point out that our operational meaning of a quasimultiple-shell acquisition is similar to multiple-shell acquisition as described above except that the points in each shell may be associated with slightly different diffusion weightings from the nominal weighting for that shell. Suppose we have three shells, with nominal b-values of 500, 1000, and 1500 $\mathrm{s/mm^2}$, and each

shell has 20 uniformly distributed measurements, a quasimultiple-shell acquisition would be an acquisition in which the 20 measurements of the first, the second, and the last shells have b-values (in units of s/mm^2) ranging from 250 to 750, 750 to 1250, and 1250 to 1750, respectively. Such an approach in designing radial measurement will ensure incoherent sampling radially while maintaining maximal angular incoherence. Next, we will develop a cost function that will identify specific points to be moved to various shells so as to satisfy criteria #1 and #2 simultaneously.

To facilitate subsequent discussion, we will introduce a convenient graphical representation as shown in Fig. 1 with the assumptions that $n_1 \geq n_2 \geq \cdots \geq n_K$ and that the first row has m_1 measurements, the second row has m_2 measurements, and so on such that $N = \sum_{i=1}^{n_1} m_i$ and $K = m_1 \geq m_2 \geq \cdots \geq m_{n_1}$. The computation of m's can be easily achieved through algorithmic approach by putting ones in the jagged grid and summing the values across the columns for each row. The points placed on the jagged grid may be taken to be any permutation from a list of N original points, $\{P_1, \ldots, P_N\}$, and the permutated list of points are denoted by P_{S_k} with a single index, S_k, with k ranges from 1 to N. Hence, the sequence, $\{S_1, S_2, S_3, \ldots, S_N\}$, is a permutation of the original sequence, $\{1, 2, 3, \ldots, N\}$. Each point, P_{S_k}, is a unit vector. For convenience, we also use the same symbol but with two indices, i.e., P_{ij}, to refer to the point located at the ith row and the jth column in Fig. 1; here, the assignment, denoted by the symbol $\leftarrow$, is made from P_{S_k} to P_{ij} in a column-wise fashion, i.e., $P_{11} \leftarrow P_{S_1}$, …, $P_{n_1 1} \leftarrow P_{S_{n_1}}$, $P_{12} \leftarrow P_{S_{n_1+1}}$, and so on with the final assignment given by $P_{n_K K} \leftarrow P_{S_N}$.

Due to the constraint and the important role of antipodal symmetry in diffusion MRI, we will also introduce a simplifying strategy by classifying points as real and their corresponding antipodal points as virtual. If we have N real points (on the upper hemisphere), denoted by unit vectors r_i with $i = 1, \ldots, N$, then the total electrostatic energy for the complete configuration of $2N$ points of both real and virtual points is given by:

$$\varphi = \tfrac{N}{2} + 2 \sum_{i=1}^{N-1} \sum_{j=i+1}^{N} \left(\frac{1}{r_{ij}} + \frac{1}{\sqrt{4 - r_{ij}^2}} \right) \tag{1}$$

with $r_{ij} \equiv \|r_i - r_j\|$. Note that Eq. (1) is expressed solely in terms of real points. If we define $S(r_i, r_j) \equiv \frac{1}{r_{ij}} + \frac{1}{\sqrt{4-r_{ij}^2}}$, then $S(r_i, r_j)$ may be thought of as a reciprocal metric (or reciprocal distance measure) between two real points. Now, we are ready to introduce the cost function, which can be express concisely as:

$$\Phi = \frac{\sum_{j=1}^{K} \left(\overbrace{\underbrace{\frac{n_j}{2} + 2 \sum_{h=1}^{n_j - 1} \sum_{i=h+1}^{n_j} S(P_{hj}, P_{ij}) - E_{n_j}}_{E_{n_j}}}^{\phi_R(j)} \right)}{\sum_{q=1}^{n_1} \left(\overbrace{\underbrace{\frac{m_q}{2} + 2 \sum_{r=1}^{m_q - 1} \sum_{s=r+1}^{m_q} S(P_{qr}, P_{qs}) - E_{m_q}}_{E_{m_q}}}^{\phi_C(q)} \right)} \tag{2}$$

The function $\phi_R(j)$ denotes the electrostatic energy of all the points in the jth column. Similarly, $\phi_C(q)$ denotes the electrostatic energy of all the points in the qth row. Note that E_n is the electrostatic energy of the most uniformly distributed antipodally symmetric point set with n number of real points. Therefore, $\tilde{\phi}_R(j)$ (or $\tilde{\phi}_C(q)$) is the relative difference between $\phi_R(j)$ and E_{n_j}(or between $\phi_C(q)$ and E_{m_q}). Minimizing Φ is equivalent to simultaneously minimizing the numerator and maximizing the denominator of Eq. (2). Minimizing the numerator is aimed at fulfilling criterion #1 while maximizing the denominator is aimed at fulfilling criterion #2. The motivation behind the use of relative difference in evaluating the electrostatic energy is to facilitate comparison among configurations of different sizes. For example, it allows us to determine whether a 5-point set is "more uniform" than a 7-point set in a quantitative and comparable manner.

Minimizing Φ is a challenging combinatorial optimization problem that requires rearrangement of points to achieve lower Φ value. It can be shown that the number of distinct configurations is $N!$, $N! \equiv n \cdot (n-1) \cdots 2 \cdot 1$ is the factorial function, if the numbers of measurements in each row and each column are distinct. For the special case when the grid is rectangular with n rows and m columns (shells), the

SHELL / INDEX	1	2	⋯	K
1	$P_{1\,1}$	$P_{1\,2}$	⋯	$P_{1\,K}$
2	$P_{2\,1}$	$P_{1\,2}$	⋯	$P_{2\,K}$
⋮	⋮	⋮	⋱	⋮
n_K	$P_{n_K 1}$	$P_{n_K 2}$	⋯	$P_{n_K K}$
⋮	⋮	⋮	⋮	
⋮	⋮	⋮	⋮	
⋮	⋮	⋮		
n_2	$P_{n_2 1}$	$P_{n_2 2}$		
n_1	$P_{n_1 1}$			

FIG. 1. A jagged grid is used as a graphical representation to manage multiple-shell design; each column of data points is a collection of points on a spherical shell. Points in each row may be thought of as collections points around a radial line.

number of configuration is given by $\frac{(m\times n)!}{m!n!}$. The number of distinct configurations is astronomical for typical values of m and n, which renders exhaustive search impractical. For example, with $m = 8$ and $n = 30$, i.e., $N = 240$, which is typical in diffusion MRI applications, the number of distinct configurations is in the order of 10^{431}. Therefore, an effective and efficient search strategy capable of finding the optimal configuration within appropriate timeframe is imperative. We will present a semistochastic and moderately greedy algorithm with simulated annealing in Sec. II.A to solve this interesting but challenging combinatorial problem whose solution will shed new light on many areas of research beyond diffusion MRI such as geosciences, imaging sciences, and notably three-dimensional radial MRI, please refer to Appendix A in which we showed how the proposed cost function and search strategy can be adapted to solve the problem of optimal view-ordering in three-dimensional radial MRI.

II.A. Semistochastic and moderately greedy combinatorial search strategy

We propose a novel search strategy to seek the optimal configuration. The algorithm is outlined below:

II.A.1. Semistochastic and moderately greedy combinatorial search algorithm

Preliminary step. Given an ordered list of N number of points, $\{P_1, \ldots, P_N\}$, obtained from tabulated data or from Refs. 31 and 42, we make a one-to-one correspondence between $\{P_1, \ldots, P_N\}$ and $\{1, 2, 3, \ldots, N\}$. It is assumed that we also have the relevant information such as the number of shells, K, and the number of measurements in each row and column, i.e., $n_1 \geq n_2 \geq \cdots \geq n_K$ and $K = m_1 \geq m_2 \geq \cdots \geq m_{n_1}$. We find the maximum and minimum values of Φ from 5000 random configurations. We then set T, which is the effective temperature to be used in our modified simulated annealing, to be five times the difference between these maximum and minimum values. The first T will be denoted by T_0.

Fill the jagged grid with a random permutation of $\{1, 2, 3, \ldots, N\}$ column by column:

Step 1: Find the index j^* for which $\tilde{\phi}_R(j)$ is maximum.

Step 2: Find the index q^* for which $\tilde{\phi}_C(q)$ is minimum.

Step 3: If $P_{q^*j^*}$ exists, we look for lower energy configuration by swapping it with other points systematically in the jagged grid. If the rearranged configuration leads to lower Φ, exit and set the "flag" to 1. If none of the rearrangements leads to lower Φ, then exit and set the flag to -1.

If $P_{q^*j^*}$ does not exist, we suggest using a point within q^*th row and a point within j^*th column and swap these points with other points in the grid. Specifically, we look for the point, P_{q^*r}, that *minimizes* the following inner sum:

$$\sum_{\substack{s=1 \\ s\neq r}}^{m_{q^*}} S(P_{q^*r}, P_{q^*s}),$$

which is equivalent to finding a point, P_{q^*r}, that is furthest away from those in the q^*th row. Similarly, we may also look for a point, P_{ij^*} that *maximizes* the following inner sum:

$$\sum_{\substack{k=1 \\ k\neq i}}^{n_{j^*}} S(P_{ij^*}, P_{kj^*}),$$

which is equivalent to finding a point, P_{ij^*}, that is closest to those in the j^*th column. Then, we can successively swap these two points, P_{q^*r} and P_{ij^*}, with all other points in the grid to search for a better configuration. If the rearranged configuration leads to lower Φ, exit and set the flag to 1. If none of the rearrangements leads to lower Φ, then exit and set the flag to -1.

Note: Step 4a and Step 4b below are alternative strategies considered in this paper but Step 4b is the strategy of choice for its effectiveness in finding optimum configuration.

Step 4a: If the flag is -1, two distinct points on the grid will be randomly selected and swapped (or two pairs of points may be randomly selected and swapped), if the rearranged configuration is better than the current configuration then we go back to Step 1; otherwise, we will perform the same operation of (internal) randomization for another 500 or more times before exiting with a flag of -1. We should note that internal randomization degrades efficiency but improves the overall quality of the search.

Step 4b: If the flag is -1, we adopt the simulated annealing approach in which configurations with higher energy (or cost function value) may still have the likelihood of being accepted if the effective temperature is high.

First, two distinct points on the grid will be randomly selected and swapped, if the rearranged configuration is better than the current configuration then we set the flag to "1" and go to Step 5; otherwise, we accept the new configuration with probability

$$\exp(-(\Phi_{new} - \Phi_{old})/T),$$

where Φ_{new} is the value of the cost function of the new configuration and Φ_{old} is that of the old configuration.

Internally, we keep a counter to ensure that no more than $100N$ trials for each value of the effective temperature in which the new configuration is accepted. If the value of the counter reaches $100N$, we reset the counter to zero and reduce the effective temperature according to the simple formula:

$$T_{n+1} = 0.9T_n,$$

where T_n is the current effective temperature and T_{n+1} is the next effective temperature to be used in simulated annealing.

Note that Step 4b will be repeated until either we find a new Φ_{new} that is truly lower than Φ_{old} and at which point we set the flag to be 1 and move on to Step 5 or the number of repetitions of Step 4b reaches a predefined number, which is the maximum iteration allowed (e.g., we used 1 000 000 for small N, say $N < 300$, and smaller value for large N), and the flag will be set to "-1".

Step 5: If the flag is 1 then repeat Steps 1–4. Otherwise, exit the algorithm.

We should note that Steps 4a and 4b are two alternative strategies and the search strategy that incorporates Step 4a is

slightly greedier and more suitable for very large sample size, say $N > 1000$, than that of the search strategy that incorporates Step 4b. Based on our numerical testing, we found that the search algorithm with Step 4b, which is based on simulated annealing, is more effective in finding the optimum solution.

Finally, we will touch on some steps that could significantly speed up the search. Since the distances between the original spherical points are fixed, we should compute and store the values of all the inverse distances, i.e., $S(P_i, P_j)$, in a form of a lower triangular matrix, see Fig. 2. It should also be clear by now that it is more efficient to consider rearrangement of the sequence, $\{S_1, S_2, S_3, \ldots, S_N\}$, in, P_{S_k}, than to actually rearrange or move the points on the grid. Therefore, the final product from the search algorithm is the optimum configuration, which is simply a grid with numbers rearranged.

II.B. Optimal ordering strategy

The key motivation behind the use of optimal ordering in diffusion MRI measurements (or gradient directions) is due in part to the desire of salvaging as much information as possible from partially completed diffusion MRI scan in the event that the scan has to be interrupted unexpectedly, e.g., see Refs. 29 and 30. Our recently proposed deterministic optimal ordering strategy for the single-shell acquisition[31] is immediately applicable to the proposed multiple-shell acquisition because of criterion #3. Here, we briefly outline the strategy of incorporating our previously proposed optimal ordering in this work. Since the points are originally placed uniformly on the same sphere, our recent deterministic optimal ordering method can be applied to the point set to create a list of optimally ordered point set, denoted by list #1, which is then fed into the semi-stochastic and moderately greedy combinatorial search algorithm proposed above. The final optimum multiple-shell acquisition, denoted by list #2, can be written out as a text file with points and their corresponding b-values or q-values listed side by side. The points in list #2 is arranged in exactly the same order as in list #1 but their corresponding b-values retrieved from the optimum configuration (or the grid, the output from the above search algorithm).

III. METHOD OF EVALUATION OF ACQUISITION DESIGNS

The approach we take in evaluating the stability of various acquisition designs is based on the condition number and the A-optimal measure of the design matrix. The use of condition number in the analysis of stability of linear inverse problem is well known, see Refs. 28, 43, and 44. To construct the design matrix, we adopt the basis functions proposed in Ref. 37. There are several proposed reconstruction techniques[35–37] but the basis functions proposed in Ref. 37 is better suited for the analysis of diffusion MR signals. We have made a few modifications to the basis functions so that the basis functions are real-valued and orthonormal.

In brief, the three-dimensional normalized q-space signal can be expressed in terms of the modified version of the orthonormal basis wave functions used in three-dimensional harmonic oscillator in quantum mechanics[37,45] as follows:

$$E(\mathbf{q}) = \sum_{N=0}^{N_{\max}} \sum_{\substack{\{l+2j=N+2\} \\ j\geq 1,\ l\geq 0}} \sum_{m=-l}^{l} a_{jlm} \Psi_{jlm}(u, \mathbf{q}) \tag{3}$$

with

$$\Psi_{jlm}(u, \mathbf{q}) = R_{jl}(u, \mathbf{q})\, Y_{lm}(\theta, \phi),$$

$$R_{jl}(u, \mathbf{q}) = \sqrt{2}(2\pi u)^{l+\frac{3}{2}} \sqrt{\frac{(j-1)!}{\Gamma(l+j+1/2)}} q^l \exp\left(-\frac{(2\pi u)^2}{2} q^2\right) L_{j-1}^{l+1/2}((2\pi u)^2 q^2),$$

$$Y_{lm}(\theta, \phi) = \begin{cases} -\sqrt{\frac{2l+1}{2\pi} \frac{(l+m)!}{(l-m)!}} \sin(m\phi) P_l^{|m|}(\cos(\theta)), & -l \leq m \leq -1 \\ \sqrt{\frac{2l+1}{4\pi}} P_l(\cos(\theta)), & m = 0 \\ \sqrt{\frac{2l+1}{2\pi} \frac{(l-m)!}{(l+m)!}} \cos(m\phi) P_l^m(\cos(\theta)), & 1 \leq m \leq l. \end{cases}$$

Note that $\mathbf{q} = q\hat{\mathbf{q}}$, $\hat{\mathbf{q}} = [\sin(\theta)\cos(\phi), \sin(\theta)\sin(\phi), \cos(\theta)]^T$, L_n^l is the generalized Laguerre polynomial of order n, P_l^m is the associated Legendre polynomial, and Γ is the Gamma function. Note also that the second summation is supposed to be evaluated for all even number $l \geq 0$ and integer $j \geq 1$ such that $l + 2j = N + 2$. Further, the definition of the real-valued spherical harmonic functions, Y_{lm}, is consistent with our previous work, see Ref. 16. Given a collection of q-vectors (measurements), it is clear that Eq. (3) with evaluation at different q-vectors can be formulated as a matrix equation of the following form,

$$\mathbf{y} = \Phi\beta,$$

where the elements of the observation vector, $\mathbf{y}$, are the q-space signal, $E(\mathbf{q})$, measured at different q-vectors, and the elements of β are the coefficients a_{jlm} in a particular order; this particular order also affects how the basis functions are ordered in the design matrix, Φ. Finally, we would like to remind the reader that the condition number of Φ is the ratio of the largest to the smallest singular values while the A-optimal measure is the matrix trace of the inverse of the moment matrix, i.e., $tr((\Phi^T\Phi)^{-1})$.

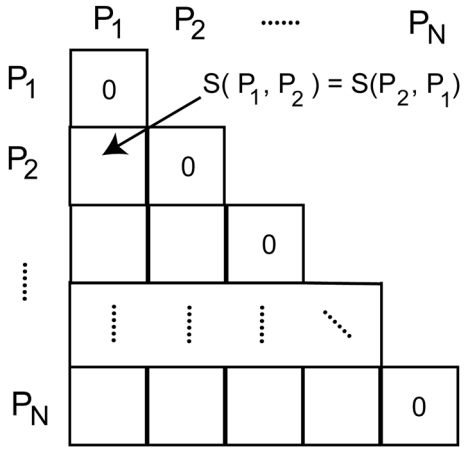

FIG. 2. Computation of the cost function is greatly simplified by the use of the metric function S between two "real" points, which is specifically designed to deal with point set that is endowed with antipodal symmetry. The lower triangular matrix shown above is used to keep the values of *S*.

IV. RESULTS

IV.A. Illustrative example

We implemented the above cost function and the proposed search strategy in Java on a machine with an Intel® Core™ i7 CPU at 1.73 GHz. We should note that the best electrostatic energy values from a single-shell configuration with different sample sizes will be needed to test our proposed approach. However, we have made available these values on the web. The first 365 configurations were iteratively optimized by using the deterministically generated antipodally symmetric point set[42] as the initial solution. The resultant electrostatic energy values have subsequently been tabulated and are available through the web, see the Acknowledgment for the URL. Electrostatic values for sample size beyond 365 are currently computed approximately from the deterministic point set. Eventually, more values beyond the first 365 will be based on point set derived from iteratively optimization.

We would like to introduce a simple and practical example to illustrate the feasibility of our approach and some important features in the results that are universal across different sample sizes. In this example, we begin with a simple 12×12 grid and generated 50 000 independent trials by filling up the grid with any random permutation drawn from (1, 2, …, 144); each number refers to the location of a point in a list of 144 iteratively optimized points generated, tabulated, and stored as a text file. We should mention that the number of distinct configurations is astronomically large and it is in the order of 10^{232}; this number is greater than the number of atoms in the observable universe, which is in the order of 10^{80}. To depend on exhaustive search to find the optimum configuration is to wait for eternity; it would still take us 10^{201} millennia if we could exhaustively search 10^{20} configurations in one second.

The distribution of the electrostatic energy of these random configurations is shown as the red histogram in Fig. 3. The proposed method (using Step 4a and with 500 internal randomization) was applied to these configurations in an attempt to minimize the electrostatic energy. The blue histogram is the resultant distribution. Please refer to the insets of Figure 3 to contrast and compare these two different histograms more closely. The lowest cost function value was 0.00369.

Separately and independently, we performed only one single trial using the proposed method with Step 4b (i.e., simulated annealing) and found that the lowest cost function value to be 0.00297. However, this single trial took approximately the same amount of time in execution, which was about 222 min 53 s, as compared to the 50 000 trials using the other alternative approach (i.e. with Step 4a). Even though the computational cost is higher, we believe the proposed method with the incorporation of simulated annealing approach in Step 4 is more effective in finding a more optimal configuration.

In what follows, we will present the point set from the most optimum configuration in two distinct perspectives. First, the points in the same column are color-coded similarly and points in different columns have distinct hues, see Fig. 4. It is clear that there is no sign of any cluster of points with the same hue. We should remind the reader that the points of the same color are on the same spherical shell and, therefore, should be as far apart from each other as possible to achieve maximal angular incoherence. Finally, the points in the same row are color-coded similarly and points in different rows have distinct hues, see Fig. 5. It is clear that we should expect to see 12 clusters of points with points in each cluster having the same hue. Again, we remind the reader that the points of the same color are, in this case, to be moved to distinct spherical sphere to achieve sufficient radial coverage or radial incoherence. This second perspective is the most stringent test of the efficacy of the cost function and of the search strategy because any discrepancy in the cluster can be easily detected by visual inspection.

Another way of inspection that is more convenient for large sample size is to investigate the variability of the values of $\phi_R(j)$ for all the columns and $\phi_C(q)$ for all the rows when the grid is rectangular, or of $\tilde{\phi}_R(j)$ and $\tilde{\phi}_C(q)$ for

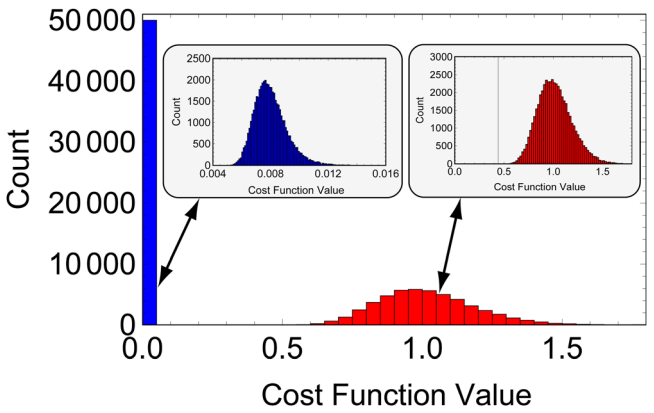

FIG. 3. 50 000 random permutations were generated to fill the 12×12 grid. The initial cost function values of these 50 000 samples are shown in the histogram that is color-coded in red. The histogram of the final cost function values of these 50 000 samples is shown in blue. Inset shows the magnified version of these two histograms.

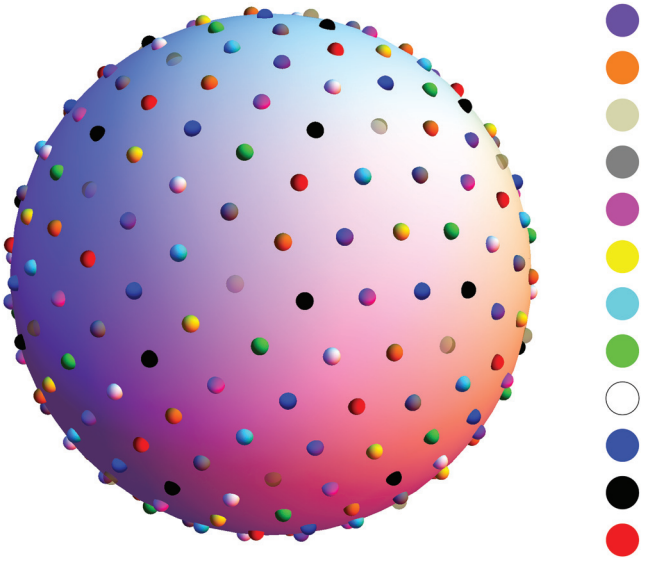

FIG. 4. The points are generated from the example of a 12×12 grid. Every point in the same shell has the same color and each shell is assigned a distinct color and these colors are shown on the right. It can be seen that each set of points with the same color is nearly uniformly distributed on the sphere, which is related to the goal of criterion #1.

jagged grid; we used this approach in another example in Appendix A.

IV.B. Evaluation of acquisition designs

For simplicity, the number of measurements was chosen to 81 to ensure that a square grid of 9×9 was one of the 18 designs considered in this investigation, see Fig. 6. We

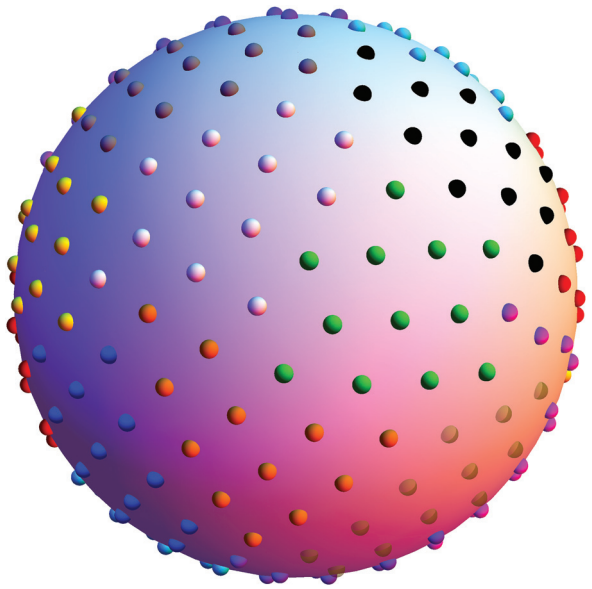

FIG. 5. The clusters seen here are generated from the example of a 12×12 grid. Each row contains points with the same color, and these points are designed to be close together in a form of a cluster so that, when the points are projected to different shells, we would have fulfilled the criterion #2, which is to provide the maximum coverage around each radial line. The problem of the boundary effect in which there might be two neighboring points with distinct colors but are moved to some common shell will not be an issue here because of criterion #1.

q-value (mm^{-1})	25.2	50.4	75.6	100.9	126.1	151.3	176.6	201.8	227.0		
Shell / Design	1	2	3	4	5	6	7	8	9	Condition Number	A-optimal measure
1	9	36	36							34.9	1.5×10^7
2	18	27	36							45.2	1.5×10^7
3	9	9	27	36						39.8	3.9×10^7
4	9	18	18	36						46.5	2.9×10^7
5	9	9	9	18	36					71.7	1.1×10^8
6	9	9	9	9	9	36				68.1	1.2×10^8
7	27	27	27							63.0	2.0×10^7
8	9	18	27	27						38.8	2.0×10^7
9	9	9	9	27	27					70.4	1.0×10^8
10	18	18	18	27						64.3	3.0×10^7
11	9	9	18	18	27					47.3	5.7×10^7
12	9	9	9	9	18	27				68.9	1.0×10^8
13	9	9	9	9	9	9	27			68.5	1.3×10^8
14	9	18	18	18	18					47.1	3.0×10^7
15	9	9	9	18	18	18				69.5	1.1×10^8
16	9	9	9	9	9	18	18			70.2	1.1×10^8
17	9	9	9	9	9	9	9	18		73.1	1.3×10^8
18	9	9	9	9	9	9	9	9	9	86.6	1.6×10^8

* Δ = 16.32 ms, D = 2.1 x 10^{-3} mm^2/s, u = 0.00827.

FIG. 6. A collection of 18 acquisition designs and the corresponding matrix condition numbers. The design matrices were constructed from the three-dimensional basis functions with $u = 0.00827$, which in turn depends on Δ and D. Here, the diffusivity is chosen to be close to free diffusion of water in the brain. For example, design #8 has (9,18,27,27) points in the (1st, 2nd, 3rd, 4th) shells, respectively. This design has matrix condition number of 38.8 and A-optimal measure of 2.0×10^7. Further, the q-value at the first shell is 25.2 mm^{-1}. Design #18 is the square acquisition design.

should note that the number of possible designs is equal to the unrestricted partitions of the integer 81, which turns out to be 18 004 327, see Ref. 46.

To construct the design matrix and evaluate its condition number for different experimental conditions, we have to have the following information:

1. A collection of measurement vectors, **q**'s. The q-values are shown in Fig. 6. In each design shown in Fig. 6, the orientation information of the measurement vectors was obtained by the method proposed in Sec. II.
2. The value of u in Eq. (3). The inherent advantage of the basis function proposed by Özarslan *et al.*[37] is that u can be associated with the Einstein relation, i.e., $u = \sqrt{2D\Delta}$, where D is the diffusion coefficient and Δ is the diffusion time. Due to heterogeneity of diffusivity in the human brain, it is important to investigate the stability of the acquisition design, i.e., the condition number of the design matrix under two very distinct values of diffusivity. Here, the two different values of the diffusion coefficient were chosen, the first one is close to the observed value of free diffusion in the human brain, which is 2.1×10^{-3} mm^2/s and the other is close to very slow diffusion (2.1×10^{-5} mm^2/s) as in the case of hindered diffusion.

q-value (mm^{-1}) / Shell / Design	25.2	50.4	75.6	100.9	126.1	151.3	176.6	201.8	227.0	Condition Number	A-optimal measure
	1	2	3	4	5	6	7	8	9		
1	9	36	36							7.6×10^3	2.0×10^{13}
2	18	27	36							7.1×10^3	2.1×10^{13}
3	9	9	27	36						1.8×10^3	2.0×10^{12}
4	9	18	18	36						2.0×10^3	2.2×10^{12}
5	9	9	9	18	36					689	4.0×10^{11}
6	9	9	9	9	9	36				319	1.1×10^{11}
7	27	27	27							7.0×10^3	2.1×10^{13}
8	9	18	27	27						1.9×10^3	2.0×10^{12}
9	9	9	9	27	27					664	3.8×10^{11}
10	18	18	18	27						2.0×10^3	2.2×10^{12}
11	9	9	18	18	27					692	3.7×10^{11}
12	9	9	9	9	18	27				308	1.0×10^{11}
13	9	9	9	9	9	9	27			159	3.1×10^{10}
14	9	18	18	18	18					761	4.0×10^{11}
15	9	9	9	18	18	18				310	1.0×10^{11}
16	9	9	9	9	9	18	18			165	3.4×10^{10}
17	9	9	9	9	9	9	9	18		93.0	1.2×10^{10}
18	9	9	9	9	9	9	9	9	9	80.3	8.8×10^9

* Δ = 16.32 ms, D = 2.1 x 10^{-5} mm^2/s, u = 0.000827.

FIG. 7. The same collection of 18 acquisition designs as in Fig. 6 but the design matrices were now constructed from the basis functions with $u = 0.000827$. Here, the value of the diffusivity was chosen to be low similar to the case of hindered diffusion.

3. The value of $N_{\max}$ was chosen to be 4, which yields exactly 22 coefficients in the series expansion in Eq. (3).

With the relevant parameters set to the chosen values, we evaluated the condition number and the A-optimal measure associated with each design shown in Fig. 6 (fast diffusion) and Fig. 7 (slow diffusion). It is clear from the results that any design closer to the square one has a lower combined A-optimal measure and design #18 (the square design) is has the lowest combined A-optimal measure. The results in Figs. 6 and 7 show that the condition numbers of designs #17 and #18 are less variable than other designs. We also investigated the behavior of the condition number of the design matrix of design #18 as a function of the diffusion time with diffusivity fixed at free diffusion, see Fig. 8. It is interesting to note that there are two minima in Fig. 8 but the minimum indicated at 16.32 ms is the one that is more practical for diffusion MRI since the diffusion time has to be much greater than the width of the diffusion gradient pulse. We would like to point out that scaling the diffusion coefficient up or down will increase the condition number of the design matrix if the diffusion time is fixed at 16.32 ms. Finally, we investigated the condition number of two design matrices derived from the radial scheme, i.e., nine uniformly distributed q-vectors on each shell and the q-values used were obtained from Fig. 6, and the DSI-like sampling scheme.[18] The condition numbers for the radial scheme were 2.5×10^{18} and 5.9×10^{16} for both cases of fast diffusion and slow diffusion, respectively. The values of the A-optimal measure for the radial scheme were 2.1×10^{23} and 1.4×10^{24} for both cases of fast diffusion and slow diffusion, respectively. The condition numbers for the DSI scheme were 3×10^{15} for the case of fast diffusion and 69.35 for the case of slow diffusion. The values of the A-optimal measure for the DSI scheme were 7×10^{30} for the case of fast diffusion and 7×10^9 for the case of slow diffusion. Both of these commonly used sampling schemes, DSI and radial, have a much higher combined value of A-optimal measure than many of the designs considered in Fig. 6. The DSI sampling scheme can be visualized as integral lattice points that are within and on some radius of integral value, which is associated with the maximum q-value. We obtained 76 lattice points with integral radius of 3 and added five more repeated measurements at the center of q-space to ensure the total number of sampling points is exactly the same as other designs considered in this work.

Finally, we note that the time taken by the proposed search strategy to find the square design (design #18) was about 18 min.

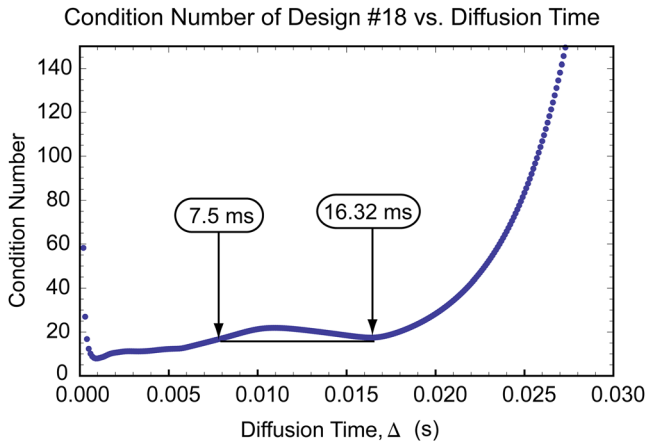

FIG. 8. The condition number of the design matrix of design #18 as a function of the diffusion time.

V. DISCUSSION

We have been grappling with the problem of the SOA design for a multiple-shell acquisition in diffusion MRI for awhile without any progress until we treaded to other territory to address the question on the optimal view-ordering in three-dimensional radial MRI. Chronologically, the solution to the three-dimensional radial MRI was found first and that of diffusion MRI later. Due to our continued interest and research effort in diffusion MRI, we have decided to present our finding in the context of diffusion MRI and made only a brief mention, in a form of an appendix, on how our proposed approach can be adapted to solving optimal view-ordering in three-dimensional radial MRI. However, we should point out that the radial scheme is less optimal than the proposed design, notably the square design, design #18 in Fig. 6.

The main objective of this work is to show the simplicity and intuitiveness of our optimality criteria for sparse

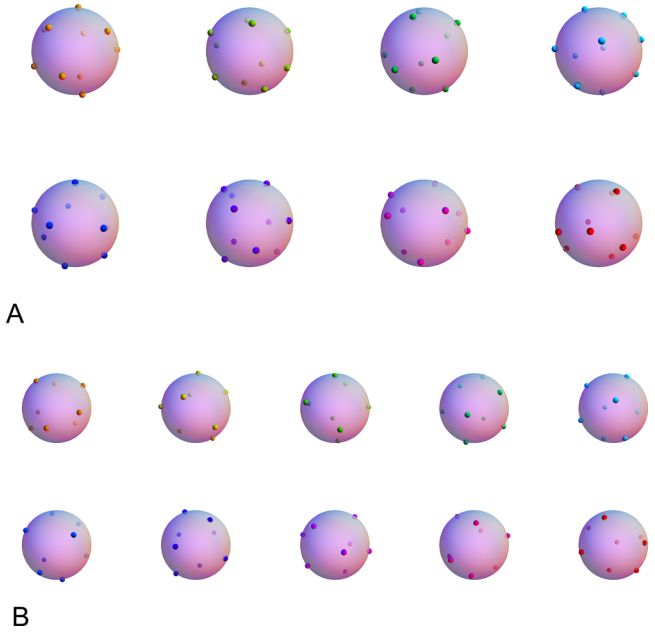

FIG. 9. (A) There are eight rows and each row of ten points is shown here as points with the same hue on the translucent unit sphere. Points in different rows have different hues. (B) There are ten columns and each column has eight points. Each column of eight points is shown here as points with the same hue on the translucent unit sphere. Again, points in different columns have different hues.

multiple-shell and quasimultiple-shell acquisitions in diffusion MRI and to share with the reader a novel search algorithm, which is based on the notion of *moderate greediness*, a term borrowed from social science. Incorporation of simulated annealing in Step 4, specifically Step 4b, of the proposed search algorithm makes the search more effective but at a higher computational cost. Simulated annealing, with its distinctive feature of being able to explore larger number of slightly less optimal configurations (with respect to a particular level of effective temperature) at higher effective temperature, and fewer and fewer of those suboptimal configurations as the effective temperature decreases, may be thought of as *measured sacrifice* to achieve coherence in socioeconomic terms. Note that the apparent coherence here in angularity will disappear once the points are moved to different shells so as to achieve better radial incoherence. Even better radial incoherence can be achieved with quasimultiple-shell design. We believe angular and radial incoherence in sampling will play an important role in diffusion MRI as the number of compressive sensing applications to diffusion MRI increases.[47]

The results are very promising, interesting, and practical for diffusion MRI acquisitions. It is interesting to note that the square design turns out to be better in terms of lower combined A-optimal measures than all the designs considered in this study and much better than the commonly used radial design, which is similar to the sampling scheme of three-dimensional radial MRI, and the DSI scheme. The key findings are that (1) the multiple-shell design similar to design #18 is better than the current paradigm of sampling on a single shell and (2) this particular multiple-shell design is also better than the multiple-shell design obtained from the radial scheme. Beyond the confine of diffusion MRI, it is very interesting to point out the following fact, which is that we managed to find an optimum configuration for a realistic example *within a realistic timeframe* even though the number of distinct configurations is astronomically large. This particular finding is most encouraging and exciting from the point of view of computational science and engineering.

Finally, we would like to mention that the proposed approach may be of relevance to other applications such as geosciences (network design of underground seismometers), geospatial intelligence (the design of multiple satellite constellations[48]), and last but not least, other biomedical imaging modalities.

ACKNOWLEDGMENTS

C.G.K. dedicates this work to Pauline Toh and Eng Khoon Leong. Software related to this work will be made available through the following URL: http://sites.google.com/site/hispeedpackets. This work was supported in part by the National Institutes of Health Grant No. IRCMH090912-01. E.Ö. was supported by the Department of Defense in the Center for Neuroscience and Regenerative Medicine (CNRM) and the Henry M. Jackson Foundation (HJF).

APPENDIX A: APPLICATION OF THE PROPOSED APPROACH TO FINDING OPTIMAL VIEW-ORDERING IN THREE-DIMENSIONAL RADIAL MRI

3D MR data are most often acquired with multiple readout windows. The inconsistency among readout windows is usually due to subject motion and variation in spin states. This inconsistency leads to image artifacts in the final reconstructed 3D volume. The nature and the magnitude or severity of the artifact are determined by the k-space trajectory and the order in which the views are acquired. The effects of view ordering have been extensively studied in 2D and 3D Cartesian MRI and 2D radial MRI.[49–54] Most existing techniques, aim to isolate signal variations for a single source (e.g. T2 decay) or along a single time dimension.

Unfortunately, the design of view ordering schemes in multiple-dimensions and/or for 3D trajectories is nontrivial. Even though 3D radial MRI (Ref. 55) is increasingly common in clinical and research studies such as MR angiography, sodium MRI, and musculoskeletal MRI,[53,56–60] the lack of an intuitive optimality criterion for designing view ordering has led to the use of various heuristic ordering schemes such as the simple interleaving method, the pseudorandom bit-reversal method,[61] and the Golden Mean method.[62] While these schemes have been shown to produce images of good quality, there is no guarantee that they are optimal.

In this appendix, we will present a novel view-ordering optimality criterion for 3D radial MRI that builds upon the proposed cost function and search strategy in the main text for finding optimal view-ordering. Our proposed method determines view ordering through optimization of a cost function. The cost function directly incorporates criteria to minimize

coherent aliasing from missing or corrupt data. The proposed method can be illustrated with a simple example drawn from 3D radial fast spin echo (FSE) imaging technique [or rapid acquisition with relaxation enhancement (RARE)].[63]

FSE has led to significant reduction in scan time with recent developments on variable refocusing flip angles,[64,65] which have made it possible to acquire MR data with very long echo trains. The reduction in scan time may also be used to improve image resolution. However, the acquisition of multiple echoes within the same excitation comes at a cost of enhanced image artifacts such as blurring or ringing because of T2 decay. T2 decay introduces signal modulation in k-space. Therefore, different view-ordering strategies[49–54] have been developed and used in an effort to make the signal modulation as incoherent as possible in k-space. Our view-ordering strategy consists of two steps. The goal of the first step is to make the signal modulation as incoherent as possible in each echo train and among the same echoes across the trains. The goal of the second step is to make the signal modulation as incoherent as possible in different echo trains and in different echoes across the trains.

Suppose that we have a set of N points uniformly distributed on the surface of the unit sphere, e.g., Ref. 66, and N is a composite number, e.g., $N = m \times n$. Here, we desire to sample N points from the set of points P, and only need to know the order in which to sample them, S. The view ordering, S, can be separated into multiple dimensions. For example, S may be split into n echo trains, each m echoes long. We can imagine placing points on an $m \times n$ grid with m rows and n columns, which is a special case of our general jagged grid in the main text.

The view ordering, S, can be determined by minimizing a cost function. In this work, we have chosen to maximize the distance between points using electrostatic potential energies along the rows and columns. The criterion can be expressed as follows:

$$\Phi_{PR} = \sum_{j=1}^{n} \left(\underbrace{\sum_{i=1}^{m-1} \sum_{k=i+1}^{m} S(P_{ij}, P_{kj})}_{\phi_R(j)} \right) + \sum_{q=1}^{m} \left(\underbrace{\sum_{r=1}^{n-1} \sum_{s=r+1}^{n} S(P_{qr}, P_{qs})}_{\phi_C(q)} \right) \tag{A1}$$

The function $\phi_R(j)$ denotes the electrostatic potential energy of all the points in different rows but in the same jth column. Similarly, $\phi_C(q)$ denotes the electrostatic potential energy of all the points in different columns but in the same qth row. Since the problem of optimal view-ordering can be solved using rectangular grid rather than jagged grid, we do not have to deal with point sets with different sizes among the rows or among the columns. Therefore, the cost function is simpler than the original cost function proposed in the main text. More importantly, due to the goals of making the signal modulation as incoherent as possible *in each echo train and among the same echoes across the trains* and *in different echo trains and in different echoes across the trains*, we have to have the two terms added as in Eq. (A1) rather than in a form of a ratio as in the original cost function Eq. (2).

Finally, the following modification should be introduced to the search algorithm in the main text:

Preliminary step: similar to the proposed algorithm in the main text.

Step 1: Find the index j^* for which $\phi_R(j)$ is maximum.

Step 2: Find the index q^* for which $\phi_C(q)$ is maximum.

Step 3: Look for lower energy configuration systematically by swapping P_{ij} and $P_{q^*j^*}$ for all $i \neq q^*$ and $j \neq j^*$. If the rearranged configuration leads to lower Φ_{PR}, exit and set the flag to 1. If none of the rearrangements leads to lower, we suggest using a point within q^*th row and a point within j^*th column and swap these points with other points in the grid. Specifically, we look for the point, P_{q^*r}, that *maximizes* the following inner sum:

$$\sum_{\substack{s=1 \\ s \neq r}}^{m} S(P_{q^*r}, P_{q^*s}).$$

Similarly, we may also look for a point, P_{ij^*} that *maximizes* the following inner sum:

$$\sum_{\substack{k=1 \\ k \neq i}}^{n} S(P_{ij^*}, P_{kj^*}).$$

Then, we can successively swap each point of the two points, P_{q^*r} and P_{ij^*}, with all other points in the grid to search for a better configuration. If the rearranged configuration leads to lower Φ, exit and set the flag to 1. If none of the rearrangements leads to lower Φ, then exit and set the flag to -1.

Steps 4 and 5: similar to the proposed algorithm shown in the main text.

Example 1

It should be clear that the cost function and the search strategy presented in this appendix and in the main text can be immediately adapted to nonantipodally symmetric point set. As an illustration, we will show visually convincing results of finding optimum configuration of a rectangular grid of 8×10. In this case, there are 4.8×10^{107} distinct configurations. The lowest energy value of Φ_{PR} with nonantipodal electrostatic energy function, i.e., each occurrence of the function $S(P_v, P_w)$ in Φ_{PR} is replaced by $1/\|P_v - P_w\|$, was found to be 468.331889. The best configuration we obtained is shown in Fig. 9 in two different views.

Example 2

Ideally, we want the points in each column (or row) to be as uniform as possible but the electrostatic energy in each column or row will likely be higher than the gold standard (or the analytically exact spiral[66]) point set of the same size. By taking the ratio of the electrostatic energy of each column (or row) to the electrostatic energy of the analytically exact spiral point set of the same size and plotting the ratios of all the columns (or rows), we can easily inspect the variability

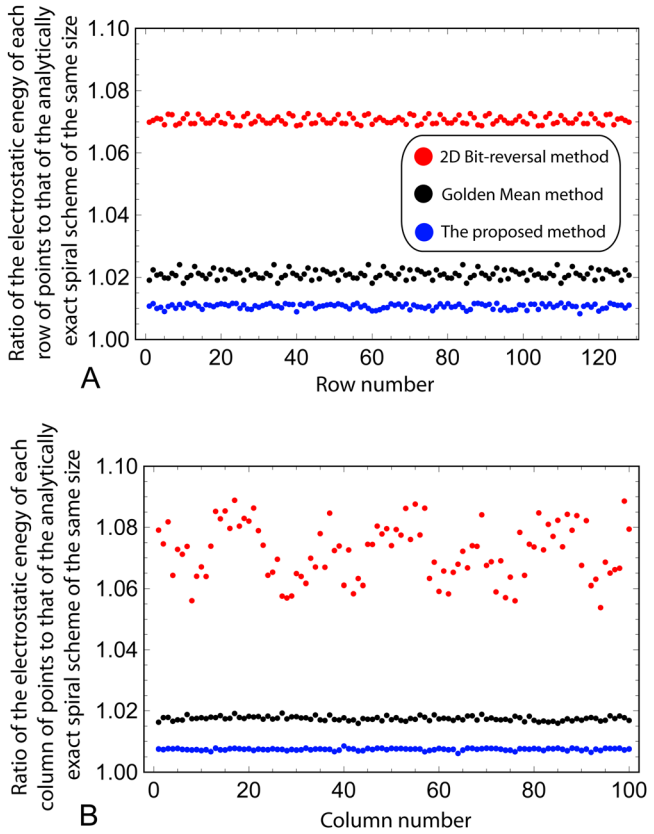

FIG. 10. (A) The ratios of the electrostatic energy of points in each row of the 2D bit-reversal method (in red or with the highest ratios), of the proposed method (in blue or with the lowest ratios) and of the Golden Mean method (in black or with the medium ratios) to that of the point set of the same size (100 points) generated from the analytically exact spiral scheme. (B) The ratios of the electrostatic energy of points in each column of the 2D bit-reversal method (in red or with the highest ratios), of the proposed method (in blue or with the lowest ratios) and of the Golden Mean method (in black or with the medium ratios) to that of the point set of the same size (128 points) generated from the analytically exact spiral scheme.

or lack thereof, which indirectly related to the uniformity, of the columns (or rows). This method of evaluation and comparison will be used in this example.

The number of points (on the sphere) as deployed in a typical 3D radial MR experiment is in the order of thousands. Here, we will use a grid of ($n = 128$, $m = 100$), which has 12 800 points and its corresponding number of distinct configurations in 10^{46642}. We will apply the method of evaluation mentioned above on our optimum point set (configuration) and on the point set obtained by the commonly used methods such as the pseudo-random bit-reversal method[61] and the Golden Mean method,[62] see Appendix B for a brief description of the 2D bit-reversal method. Based on the results shown in Fig. 10, it is encouraging to see that the electrostatic energies of the proposed point set are less variable (in row or in column) and lower than those of the 2D bit-reversal method and the Golden Mean method. We also provided a more geometric comparison regarding the variability of the Voronoi areas and of the Voronoi circumferences of our point set and the Golden Mean method, which is known to be less uniform in distribution and hence higher variability in the above geometric measures, see Fig. 11. Please refer to Appendix C in which we show how we computed the average area and circumference of the spherical cap to get a rough approximation of the lower bound of the Voronoi circumference and the average value of the Voronoi area.

APPENDIX B: 2D BIT-REVERSAL METHOD

For convenience, we include here a description of the 2D bit-reversal method. We assume the procedure of bit-reversal of an array of numbers is understood. Given a grid of m by n and an array of ordered numbers from 0 to m − 1. First, bit-reverse this array and place it in the first column. Subsequently, the value of each component of the jth column is equal to the corresponding component of the first column with $((j-1)m)$ added to it. Second, bit-reverse the array of

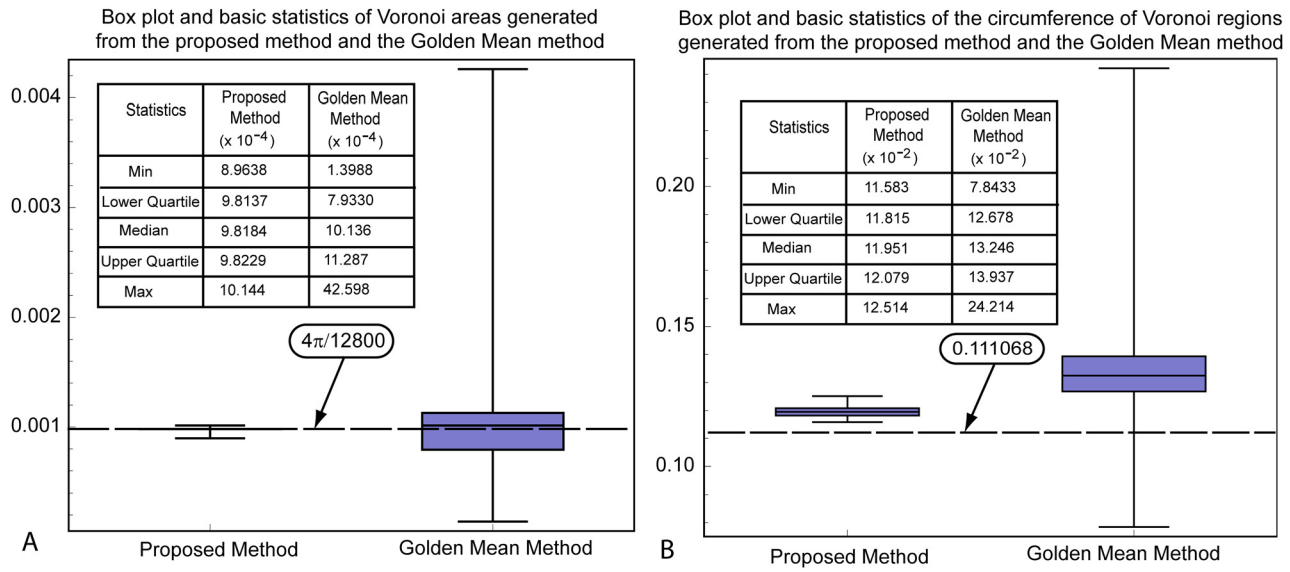

FIG. 11. Box plots and basic statistics on the Voronoi areas (A) and circumferences (B) generated from the proposed method (analytically exact spiral scheme) and the Golden Mean method.

numbers in each row then, for each kth row, cyclically shift the elements by k positions from right to left. The final grid is the desired solution of the 2D bit-reversal method.

APPENDIX C: AREA AND CIRCUMFERENCE OF A CIRCULAR CAP ON THE SPHERE

In this appendix, we present a simple expression of the circumference of a circular cone as a function of its area, which was used in Fig. 11. Our derivation is built upon our previous work, i.e., page 839 of Ref. 15. The unnormalized areal and circumferential measures for the case of the circular cone are given, respectively, by:

$$\Gamma = 2\pi\left(1 - 1/\sqrt{1+r^2}\right)$$

and

$$\Lambda = 2\pi\left(r/\sqrt{1+r^2}\right),$$

where r is the radius of the circular cone lying on the plane that is perpendicular to the unit sphere and the center of the cone is the point of contact between the plane and the unit sphere. After some manipulation, it can be shown that:

$$\Lambda = \sqrt{\Gamma(4\pi - \Gamma)}.$$

For example, if we assume that $\Gamma = 4\pi/12\,800$ then $\Lambda = 0.111068$. From the isoperimetric problems in calculus of variations, we know that a circle is the closed plane curve of a given length that encloses the largest area, and a circle is also the closed plane curve of the minimum length that encloses a given area. In fact, similar extension can be made about the surface area and the volume of the sphere, see e.g., page 224 of Ref. 67. Therefore, the circumference, Λ, represents the minimum circumference and can serve as a lower bound for evaluating the quality of the Voronoi regions.

[a]Author to whom correspondence should be addressed. Electronic mail: cgkoay@wisc.edu

[1]C. Pierpaoli, P. Jezzard, P. J. Basser, A. Barnett, and G. Di Chiro, "Diffusion tensor MR imaging of the human brain," Radiology **201**, 637–648 (1996).
[2]D. Le Bihan, E. Breton, D. Lallemand, P. Grenier, E. Cabanis, and M. Lavaljeantet, "MR imaging of intravoxel incoherent motions—Application to diffusion and perfusion in neurologic disorders," Radiology **161**, 401–407 (1986).
[3]P. J. Basser, J. Mattiello, and D. Le Bihan, "MR diffusion tensor spectroscopy and imaging," Biophys. J. **66**, 259–267 (1994).
[4]K. O. Lim, M. Hedehus, M. Moseley, A. de Crespigny, E. V. Sullivan, and A. Pfefferbaum, "Compromised white matter tract integrity in schizophrenia inferred from diffusion tensor imaging," Arch. Gen. Psychiatry **56**, 367–374 (1999).
[5]S. Mori, K. Frederiksen, P. C. M. van Zijl, B. Stieltjes, M. A. Kraut, M. Solaiyappan, and M. G. Pomper, "Brain white matter anatomy of tumor patients evaluated with diffusion tensor imaging," Ann. Neurol. **51**, 377–380 (2002).
[6]E. Hutchinson, D. Pulsipher, K. Dabbs, A. M. y Gutierrez, R. Sheth, J. Jones, M. Seidenberg, E. Meyerand, and B. Hermann, "Children with new-onset epilepsy exhibit diffusion abnormalities in cerebral white matter in the absence of volumetric differences," Epilepsy Res. **88**, 208–214 (2010).
[7]A. L. Alexander, J. E. Lee, M. Lazar, R. Boudos, M. B. DuBray, T. R. Oakes, J. N. Miller, J. Lu, E.-K. Jeong, W. M. McMahon, E. D. Bigler, and J. E. Lainhart, "Diffusion tensor imaging of the corpus callosum in Autism," Neuroimage **34**, 61–73 (2007).
[8]Y. Assaf, D. Ben-Bashat, J. Chapman, S. Peled, I. E. Biton, M. Kafri, Y. Segev, T. Hendler, A. D. Korczyn, M. Graif, and Y. Cohen, "High b-value q-space analyzed diffusion-weighted MRI: Application to multiple sclerosis," Magn. Reson. Med. **47**, 115–126 (2002).
[9]S. Ogawa, T. M. Lee, A. R. Kay, and D. W. Tank, "Brain magnetic resonance imaging with contrast dependent on blood oxygenation," Proc. Natl. Acad. Sci. U. S. A. **87**, 9868–9872 (1990).
[10]O. Sporns, G. Tononi, and R. Kötter, "The human connectome: A structural description of the human brain," PLoS Comput. Biol. **1**, e42 (2005).
[11]B. B. Biswal, M. Mennes, X.-N. Zuo, S. Gohel, C. Kelly, S. M. Smith, C. F. Beckmann, J. S. Adelstein, R. L. Buckner, S. Colcombe, A.-M. Dogonowski, M. Ernst, D. Fair, M. Hampson, M. J. Hoptman, J. S. Hyde, V. J. Kiviniemi, R. Kötter, S.-J. Li, C.-P. Lin, M. J. Lowe, C. Mackay, D. J. Madden, K. H. Madsen, D. S. Margulies, H. S. Mayberg, K. McMahon, C. S. Monk, S. H. Mostofsky, B. J. Nagel, J. J. Pekar, S. J. Peltier, S. E. Petersen, V. Riedl, S. A. R. B. Rombouts, B. Rypma, B. L. Schlaggar, S. Schmidt, R. D. Seidler, G. J. Siegle, C. Sorg, G.-J. Teng, J. Veijola, A. Villringer, M. Walter, L. Wang, X.-C. Weng, S. Whitfield-Gabrieli, P. Williamson, C. Windischberger, Y.-F. Zang, H.-Y. Zhang, F. X. Castellanos, and M. P. Milham, "Toward discovery science of human brain function," Proc. Natl. Acad. Sci. U. S. A. **107**, 4734–4739 (2010).
[12]C. G. Koay, L. C. Chang, J. D. Carew, C. Pierpaoli, and P. J. Basser, "A unifying theoretical and algorithmic framework for least squares methods of estimation in diffusion tensor imaging," J. Magn. Reson. **182**, 115–125 (2006).
[13]C. G. Koay, L. C. Chang, C. Pierpaoli, and P. J. Basser, "Error propagation framework for diffusion tensor imaging via diffusion tensor representations," IEEE Trans. Med. Imaging **26**, 1017–1034 (2007).
[14]C. G. Koay, L.-C. Chang, J. D. Carew, C. Pierpaoli, and P. J. Basser, "A unifying theoretical and algorithmic framework for least squares methods of estimation in diffusion tensor imaging," J. Magn. Reson. **182**, 115–125 (2006).
[15]C. G. Koay, U. Nevo, L. C. Chang, C. Pierpaoli, and P. J. Basser, "The elliptical cone of uncertainty and its normalized measures in diffusion tensor imaging," IEEE Trans. Med. Imaging **27**, 834–846 (2008).
[16]C. G. Koay, E. Özarslan, and P. J. Basser, "A signal transformational framework for breaking the noise floor and its applications in MRI," J. Magn. Reson. **197**, 108–119 (2009).
[17]C. G. Koay, E. Özarslan, and C. Pierpaoli, "Probabilistic Identification and Estimation Noise (PIESNO): A self-consistent approach and its applications in MRI," J. Magn. Reson. **199**, 94–103 (2009).
[18]V. J. Wedeen, T. G. Reese, D. S. Tuch, M. R. Weigel, J.-G. Dou, R. M. Weisskoff, and D. Chessler, "Mapping fiber orientation spectra in cerebral white matter with Fourier-transform diffusion MRI," Presented at the Proceedings of the 8th Annual Meeting of ISMRM, Denver, 2002.
[19]D. S. Tuch, "Q-ball imaging," Magn. Reson. Med. **52**, 1358–1372 (2004).
[20]D. S. Tuch, T. G. Reese, M. R. Wiegell, N. Makris, J. W. Belliveau, and V. J. Wedeen, "High angular resolution diffusion imaging reveals intravoxel white matter fiber heterogeneity," Magn. Reson. Med. **48**, 577–582 (2002).
[21]A. W. Anderson, "Measurement of fiber orientation distributions using high angular resolution diffusion imaging," Magn. Reson. Med. **54**, 1194–1206 (2005).
[22]E. Özarslan and T. H. Mareci, "Generalized diffusion tensor imaging and analytical relationships between diffusion tensor imaging and high angular resolution diffusion imaging," Magn. Reson. Med. **50**, 955–965 (2003).
[23]E. Özarslan, T. M. Shepherd, B. C. Vemuri, S. J. Blackband, and T. H. Mareci, "Resolution of complex tissue microarchitecture using the diffusion orientation transform (DOT)," Neuroimage **31**, 1086–1103 (2006).
[24]M. Descoteaux, E. Angelino, S. Fitzgibbons, and R. Deriche, "Regularized, fast, and robust analytical Q-ball imaging," Magn. Reson. Med. **58**, 497–510 (2007).
[25]D. C. Alexander, G. J. Barker, and S. R. Arridge, "Detection and modeling of non-Gaussian apparent diffusion coefficient profiles in human brain data," Magn. Reson. Med. **48**, 331–340 (2002).
[26]D. K. Jones, M. A. Horsfield, and A. Simmons, "Optimal strategies for measuring diffusion in anisotropic systems by magnetic resonance imaging," Magn. Reson. Med. **42**, 515–525 (1999).
[27]K. M. Hasan, D. L. Parker, and A. L. Alexander, "Comparison of gradient encoding schemes for diffusion-tensor MRI," J. Magn. Reson. Imaging **13**, 769–780 (2001).

[28]S. Skare, M. Hedehus, M. E. Moseley, and T.-Q. Li, "Condition number as a measure of noise performance of diffusion tensor data acquisition schemes with MRI," J. Magn. Reson. **147**, 340–352 (2000).
[29]J. Dubois, C. Poupon, F. Lethimonnier, and D. Le Bihan, "Optimized diffusion gradient orientation schemes for corrupted clinical DTI data sets," Magn. Reson. Mater. Phys., Biol. Med. **19**, 134–143 (2006).
[30]P. A. Cook, M. Symms, P. A. Boulby, and D. C. Alexander, "Optimal acquisition orders of diffusion-weighted MRI measurements," J. Magn. Reson. Imaging **25**, 1051–1058 (2007).
[31]C. G. Koay, S. A. Hurley, and M. E. Meyerand, "Extremely efficient and deterministic approach to generating optimal ordering of diffusion MRI measurements," Med. Phys. **38**, 4795–4801 (2011).
[32]M. Lustig, D. Donoho, and J. M. Pauly, "Sparse MRI: The application of compressed sensing for rapid MR imaging," Magn. Reson. Med. **58**, 1182–1195 (2007).
[33]D. L. Donoho, "Compressed sensing," IEEE Trans. Inform. Theory **52**, 1289–1306 (2006).
[34]E. J. Candes, J. Romberg, and T. Tao, "Robust uncertainty principles: exact signal reconstruction from highly incomplete frequency information," IEEE Trans. Inform. Theory **52**, 489–509 (2006).
[35]H.-E. Assemlal, D. Tschumperlé, L. Brun, and K. Siddiqi, "Recent advances in diffusion MRI modeling: Angular and radial reconstruction," Med. Image Anal. **15**, 369–396 (2011).
[36]M. Descoteaux, R. Deriche, D. Le Bihan, J.-F. Mangin, and C. Poupon, "Multiple q-shell diffusion propagator imaging," Med. Image Anal. **15**, 603–621 (2011).
[37]E. Özarslan, C. G. Koay, T. M. Shepherd, S. J. Blackband, and P. J. Basser, "Simple harmonic oscillator based reconstruction and estimation for three-dimensional q-space MRI," in *Proc. Intl. Soc. Mag. Reson. Med.*, 17, Honolulu, HI, 2009, p. 1396.
[38]Y. C. Wu and A. L. Alexander, "Hybrid diffusion imaging," Neuroimage **36**, 617–629 (2007).
[39]S. Kirkpatrick, C. D. Gelatt, and M. P. Vecchi, "Optimization by simulated annealing," Science **220**, 671–680 (1983).
[40]P. T. Callaghan, *Principles of Nuclear Magnetic Resonance Microscopy* (Oxford University, New York, 1991).
[41]V. V. Fedorov, *Theory of Optimal Experiments* (Academic, New York, 1972).
[42]C. G. Koay, "A simple scheme for generating nearly uniform distribution of antipodally symmetric points on the unit sphere," J. Comput. Sci. **2**, 376–380 (2011).
[43]G. H. Golub and C. F. Van Loan, *Matrix Computation*, 3rd ed. (The Johns Hopkins University, Baltimore, MD, 1996).
[44]M. Bertero and P. Boccacci, *Introduction to Inverse Problems in Imaging*. (Institute of Physics Publishing, Philadelphia, PA, 1998).
[45]B. C. Carlson, *Special Functions of Applied Mathematics* (Academic, New York, 1977).
[46]S. Wolfram, *The Mathematica Book*, 5th ed. (Wolfram Media, Champaign, 2003).
[47]Y. Rathi, O. Michailovich, K. Setsompop, S. Bouix, M. Shenton, and C. Westin, "Sparse multi-shell diffusion imaging, medical image computing and computer-assisted intervention – MICCAI 2011," Vol. 6892, edited by G. Fichtinger, A. Martel, and T. Peters (Springer, Berlin/Heidelberg, 2011), pp. 58–65.
[48]D. C. Beste, "Design of satellite constellations for optimal continuous coverage," IEEE Trans. Aerosp. Electron. Syst. **AES-14**, 466–473 (1978).
[49]R. F. Busse, A. C. S. Brau, A. Vu, C. R. Michelich, E. Bayram, R. Kijowski, S. B. Reeder, and H. A. Rowley, "Effects of refocusing flip angle modulation and view ordering in 3D fast spin echo," Magn. Reson. Med. **60**, 640–649 (2008).
[50]R. F. Busse, D. G. Kruger, J. P. Debbins, S. B. Fain, and S. J. Riederer, "A flexible view ordering technique for high-quality real-time 2DFT MR fluoroscopy," Magn. Reson. Med. **42**, 69–81 (1999).
[51]T. D. Nguyen, G. Ding, R. Watts, and Y. Wang, "Optimization of view ordering for motion artifact suppression," Magn. Reson. Imaging **19**, 951–957 (2001).
[52]R. J. Theilmann, A. F. Gmitro, M. I. Altbach, and T. P. Trouard, "View-ordering in radial fast spin-echo imaging," Magn. Reson. Med. **51**, 768–774 (2004).
[53]J. Liu, M. J. Redmond, E. K. Brodsky, A. L. Alexander, A. Lu, F. J. Thornton, M. J. Schulte, T. M. Grist, J. G. Pipe, and W. F. Block, "Generation and visualization of four-dimensional MR angiography data using an undersampled 3-D projection trajectory," IEEE Trans. Med. Imaging **25**, 148–157 (2006).
[54]A. H. Wilman, S. J. Riederer, B. F. King, J. P. Debbins, P. J. Rossman, and R. L. Ehman, "Fluoroscopically triggered contrast-enhanced three-dimensional MR angiography with elliptical centric view order: application to the renal arteries," Radiology **205**, 137–146 (1997).
[55]C. M. Lai and P. C. Lauterbur, "True 3-dimensional image-reconstruction by nuclear magnetic-resonance zeugmatography," Phys. Med. Biol. **26**, 851–856 (1981).
[56]C. A. Mistretta, O. Wieben, J. Velikina, W. Block, J. Perry, Y. Wu, and K. Johnson, "Highly constrained backprojection for time-resolved MRI," Magn. Reson. Med. **55**, 30–40 (2006).
[57]A. V. Barger, W. F. Block, Y. Toropov, T. M. Grist, and C. A. Mistretta, "Time-resolved contrast-enhanced imaging with isotropic resolution and broad coverage using an undersampled 3D projection trajectory," Magn. Reson. Med. **48**, 297–305 (2002).
[58]C. Stehning, P. Börnert, K. Nehrke, H. Eggers, and O. Dössel, "Fast isotropic volumetric coronary MR angiography using free-breathing 3D radial balanced FFE acquisition," Magn. Reson. Med. **52**, 197–203 (2004).
[59]A. M. Nagel, F. B. Laun, M.-A. Weber, C. Matthies, W. Semmler, and L. R. Schad, "Sodium MRI using a density-adapted 3D radial acquisition technique," Magn. Reson. Med. **62**, 1565–1573 (2009).
[60]J. Rahmer, P. Börnert, J. Groen, and C. Bos, "Three-dimensional radial ultrashort echo-time imaging with T2 adapted sampling," Magn. Reson. Med. **55**, 1075–1082 (2006).
[61]H. K. Song and L. Dougherty, "Dynamic MRI with projection reconstruction and KWIC processing for simultaneous high spatial and temporal resolution," Magn. Reson. Med. **52**, 815–824 (2004).
[62]R. W. Chan, E. A. Ramsay, C. H. Cunningham, and D. B. Plewes, "Temporal stability of adaptive 3D radial MRI using multidimensional golden means," Magn. Reson. Med. **61**, 354–363 (2009).
[63]J. Hennig, A. Nauerth, and H. Friedburg, "RARE imaging: A fast imaging method for clinical MR," Magn. Reson. Med. **3**, 823–833 (1986).
[64]J. Hennig, M. Weigel, and K. Scheffler, "Multiecho sequences with variable refocusing flip angles: Optimization of signal behavior using smooth transitions between pseudo steady states (TRAPS)," Magn. Reson. Med. **49**, 527–535 (2003).
[65]R. F. Busse, H. Hariharan, A. Vu, and J. H. Brittain, "Fast spin echo sequences with very long echo trains: Design of variable refocusing flip angle schedules and generation of clinical T2 contrast," Magn. Reson. Med. **55**, 1030–1037 (2006).
[66]C. G. Koay, "Analytically exact spiral scheme for generating uniformly distributed points on the unit sphere," J. Comput. Sci. **2**, 88–91 (2011).
[67]D. Hilbert and S. Cohn-Vossen, *Geometry and Imagination* (Chelsea, New York, 1952).